Remote Sensing of Environment 128 (2013) 276–288

Contents lists available at SciVerse ScienceDirect

Remote Sensing of Environment

journal homepage: www.elsevier.com/locate/rse

Analysis of directional effects on atmospheric correction

B. Franch [a,*], E.F. Vermote [b], J.A. Sobrino [a], E. Fédèle [b]

[a] Global Change Unit, Image Processing Laboratory (UCG-IPL), Parque Cientifico, Universitat de Valencia, Spain
[b] Department of Geography, 2181 LeFrak Hall, University of Maryland, College Park MD, United States

ARTICLE INFO

Article history:
Received 10 July 2012
Received in revised form 22 October 2012
Accepted 24 October 2012
Available online 12 November 2012

Keywords:
MODIS
BRDF
Albedo
6S

ABSTRACT

Atmospheric correction in the Visible and Near Infrared (VNIR) spectral range of remotely sensed data is significantly simplified if we assume a Lambertian target. However, natural surfaces are anisotropic. Therefore, this assumption will introduce an error in surface directional reflectance estimates and consequently in the estimation of vegetation indexes such as the Normalized Difference Vegetation Index (NDVI) and the surface albedo retrieval. In this paper we evaluate the influence of directional effects on the atmospheric correction and its impact in the NDVI and albedo estimation. First, we derived the NDVI and surface albedo from data corrected assuming a Lambertian surface, then by using the BRDF model parameters used in the albedo retrieval, we account for the coupling effect and retrieved an improved NDVI and albedo. The study used Climate Modeling Grid (CMG) MODIS data, which has a spatial resolution of 0.05°. We focused our analysis on four Aeronet sites located in the United States of America: KONZA EDC (a prairie region in the Flint Hills, Kansas), Howland (a forest area in Maine), Walker Branch (a forest area in Tennessee) and GSFC (at NASA's Goddard Space Flight Center). The results indicate that the relative errors due to the Lambertian assumption on the surface reflectance are 3–12% in the visible and 0.7–5.0% in the near-infrared, around 1% on the NDVI and less than 1% on the albedo.

1. Introduction

Atmospheric correction is the process by which the perturbation of the remotely sensed signal due to atmospheric effects is removed. It is essential for the estimation of physical derived parameters or in order to analyze multitemporal data. Therefore, it is important to apply this process as accurately as possible. It is well known that the majority of land surfaces are anisotropic reflectors (e.g., Barnsley et al., 1997). This directional dependence of the land reflectance as a function of the sun–target–sensor geometry is described by the Bi-directional Reflectance Distribution Function (BRDF). However, atmospheric correction methods usually assume that the surface is uniform and Lambertian (Vermote & Kotchenova, 2008). In this paper, we will estimate the error introduced when not considering the surface directional effects in the atmospheric correction scheme.

Previous works, such as Lee and Kaufman (1986) studied the effects of surface anisotropy on the derivation of surface reflectance, and on the vegetation index. Their results were based on three types of vegetation: savannah, pasture and coniferous forests from the Kriebel (1978) dataset. They concluded that the Lambertian assumption can be used satisfactorily for a view zenith angle outside the backscattering region. Hu et al. (1999) analyzed also this issue but for MODerate Resolution Imaging Spectroradiometer (MODIS) simulated data. They considered four typical land cover types: a plowed field (barren), a field of hard wheat, a grass lawn and a hardwood forest. Their results showed errors of 3–7% in the red and 2–5% in the near-infrared spectral regions, with worst cases showing errors of up to 10–20%. They observed that the further away from isotropy the BRDF shape is, and the larger the aerosol optical depth, the larger error becomes. Additionally, they obtained albedo errors between 1 and 2% in the red and near-infrared, with worst cases showing errors of up to 5%. These results were also validated by Lyapustin (1999), who computed relative albedo errors between 1 and 2%, though in one case, it reached 7%. All these works, though, used radiative transfer simulations over in situ measurements or simulated observation data, but none of them used remotely sensed data. However, Wang et al. (2010) worked with AERONET-based Surface Reflectance Validation Network (ASRVN) data which is an automated data collection and processing system (Lyapustin et al., 2006; Wang et al., 2009). It receives 50×50 km^2 subsets of MODIS L1B data from MODIS adaptive processing system (MODAPS) and Aerosol Robotic Network (AERONET, Holben et al., 1998) aerosol and water vapor information and performs atmospheric correction for about 100 AERONET sites based on accurate radiative transfer theory with complex quality control of the input data. They observed that uncompensated atmospheric scattering caused by the Lambertian model systematically biases the results, underestimating the reflectance at high solar or view zenith angles and overestimating it at low zenith angles. Their results showed that the bias in the surface reflectance can be as high as 15% in the red band and 40% in the green band. These values, though, were higher than the estimations of Hu et al. (1999). Regarding the albedo their average difference was about 0.008 in the green, 0.005 in the red and

* Corresponding author. Tel.: +34 963544054.
E-mail address: belen.franch@uv.es (B. Franch).

0034-4257/$ – see front matter © 2012 Elsevier Inc. All rights reserved.
http://dx.doi.org/10.1016/j.rse.2012.10.018

0.004 in the near-infrared bands, concluding that the albedo product of MODIS presents a low but systematic negative bias due to the Lambertian assumption.

In this paper we evaluate the influence of the Lambertian assumption when estimating both the surface reflectance and the surface albedo. Additionally, we will analyze the influence of the BRDF correction on the Normalized Difference Vegetation Index (NDVI). If this index is not correct atmospherically, its value will be degraded by reducing the contrast between the red and near infrared (NIR) reflected signals. The red signal normally increases as a result of scattered, upwelling path radiance contributions from the atmosphere, while the NIR signal tends to decrease as a result of atmospheric attenuation associated with scattering and water vapor absorption. The net result is a drop in the NDVI signal and an underestimation of the amount of vegetation at the surface (Huete et al., 1999). However, if the signal is corrected atmospherically with the Lambertian assumption, the degradation in the NDVI value will depend on how the surface anisotropy influences each spectral range.

This study was carried out using the radiative transfer code 6S (Vermote et al., 2006). We focus our analysis on MODIS CMG Collection 6 data, which have improvements to the cloud mask and atmospheric profile algorithms regarding Collection 5 data. Therefore, although we also work with MODIS data, the database is not exactly the same as Wang et al. (2010) since they correct MODIS L1B data with their algorithm while in this paper we work directly with the MODIS official product. We will center the analysis on four different surfaces: a prairie region, a broadleaf forest, a boreal–northern hardwood transitional forest and a mixed pixel of vegetation and urban residential areas.

2. Material and methodology

2.1. Study areas and dataset

This study used the MODIS Climate Modeling Grid (CMG) surface reflectance Collection 6 data (M{OY}DCMG) which are gridded in the linear latitude, longitude projection at 0.05° resolution. Science Data Sets provided for this product include surface reflectance values for Bands 1–7, brightness temperatures for Bands 20, 21, 31, and 32,

Fig. 1. Study sites: a) KONZA EDC, b) Walker Branch, c) Howland and d) GSFC.

solar and view zenith angles, relative azimuth angle, ozone, granule time, quality assessment, cloud mask, aerosol optical thickness at 550 nm and water vapor content. We analyzed daily data from both Aqua and Terra platforms between 2003 and 2006 at four different Aeronet sites (each one of them corresponded to one CMG pixel) located in the United States of America (Fig. 1): KONZA EDC (39.10°N, 96.60°W) which is a prairie region whose land cover type is grass, Walker Branch (36.0°N, 84.30°W) a broadleaf forest, Howland (45.20°N, 68.75°W) a boreal–northern hardwood transitional forest and GSFC (39.00°N, 76.85°W) which is a mixture of vegetation and urban residential areas. Additional information about these sites can be found in Morisette et al. (2002).

2.2. Methodology

The reflectance in the solar spectrum which reaches the MODIS instrument at the top of the atmosphere, valid for Lambertian surface reflectance, can be described as (Vermote & Vermeulen, 1999):

$$\rho_{sensor}(\mu_s,\mu_v,\phi)=\rho_0(\mu_s,\mu_v,\phi)+\frac{T(\mu_s)T(\mu_v)\rho_{surf}}{1-\rho_{surf}S} \tag{1}$$

where ρ_{sensor} is the reflectance received by the satellite at the top of the atmosphere, ρ_0 is the path radiance in reflectance units, $T(\mu_s)$ is the total transmittance from the top of the atmosphere to the ground along the path of the incoming solar beam, $T(\mu_v)$ is the total transmittance from the ground to the top of the atmosphere in the view direction of the satellite, ρ_{surf} is the surface reflectance with no atmosphere above it, S is the reflectance of the atmosphere for isotropic light entering the base of the atmosphere, μ_s is the cosine of the solar zenith angle, μ_v is the cosine of the view angle and ϕ is the azimuthal difference between the two azimuth angles. T is divided into a direct and diffusive part such that

$$T(\mu)=e^{-\tau/\mu}+t_d(\mu) \tag{2}$$

and likewise for $T(\mu_s)$, where τ is the total optical thickness and t_d the diffuse transmittance. If the surface is non-Lambertian, the result of the correction using Eq. (1) is inexact, due to the coupling between the surface BRDF and atmospheric radiative transfer not being taken into account (Lee & Kaufman, 1986). An approach to model this effect that stems from the work of Tanré et al. (1983) has been implemented in the 6S code as (Vermote et al., 1997):

$$\rho_{sensor}(\mu_s,\mu_v,\phi)=t_g(\mu_s,\mu_v)\left[\rho_o(\mu_s,\mu_v,\phi)+e^{\frac{-\tau}{\mu_s}}e^{\frac{-\tau}{\mu_v}}\rho_{surf}(\mu_s,\mu_v,\phi)+e^{\frac{-\tau}{\mu_v}}t_d(\mu_s)\overline{\rho}\right.$$
$$\left.+e^{\frac{-\tau}{\mu_s}}t_d(\mu_v)\overline{\rho'}+t_d(\mu_s)t_d(\mu_v)\overline{\overline{\rho}}+\frac{\left[e^{\frac{-\tau}{\mu_s}}+t_d(\mu_s)\right]\left[e^{\frac{-\tau}{\mu_v}}+t_d(\mu_v)\right]S\left(\overline{\overline{\rho}}\right)^2}{1-S\overline{\overline{\rho}}}\right] \tag{3}$$

where t_g is the transmittance due to gasses, $e^{-\tau/\mu_s}$ and $t_d(\mu_s)$ are the downward direct and diffuse transmittances of the atmosphere along the path of the incoming solar beam, $e^{-\tau/\mu_v}$ and $t_d(\mu_v)$ are the upward direct and diffuse transmittances of the atmosphere in the viewing direction, $\overline{\rho}$, $\overline{\rho'}$ and $\overline{\overline{\rho}}$ are the surface hemispherical–directional, directional–hemispherical and hemispherical–hemispherical reflectances, respectively. These latter terms are also called coupling terms, as they are responsible for the coupling between atmospheric radiative transfer with the surface reflectance properties. They are written as

$$\overline{\rho}=\frac{\int_0^{2\pi}\int_0^1\mu L^{\downarrow}_{R+A}\left(\tau_A,\tau_R,\mu_s,\mu_v,\phi'\right)\rho_{surf}\left(\mu_s,\mu_v,\phi'-\phi\right)d\mu d\phi'}{\int_0^{2\pi}\int_0^1\mu L^{\downarrow}_{R+A}\left(\tau_A,\tau_R,\mu_s,\mu_v,\phi'\right)d\mu d\phi'} \tag{4}$$

$$\overline{\rho'}(\mu_s,\mu_v,\phi)=\overline{\rho}(\mu_v,\mu_s,\phi) \tag{5}$$

$$\overline{\overline{\rho}}=\overline{\overline{\rho'}(\mu_s,\mu_v,\phi)} \tag{6}$$

$$\overline{\overline{\rho}}\approx\frac{\int_0^1\int_0^{2\pi}\int_0^1\rho_{surf}\left(\mu,\mu',\phi\right)\mu\mu'd\mu'd\mu d\phi}{\int_0^1\int_0^{2\pi}\int_0^1\mu\mu'd\mu'd\mu d\phi} \tag{7}$$

where $L^{\downarrow}_{R+A}(\tau_A,\tau_R,\mu_s,\mu_v,\phi')$ is the downward diffuse irradiance with the Sun at μ_s and τ_R (resp. τ_A) are the Rayleigh (resp. aerosol) optical depth

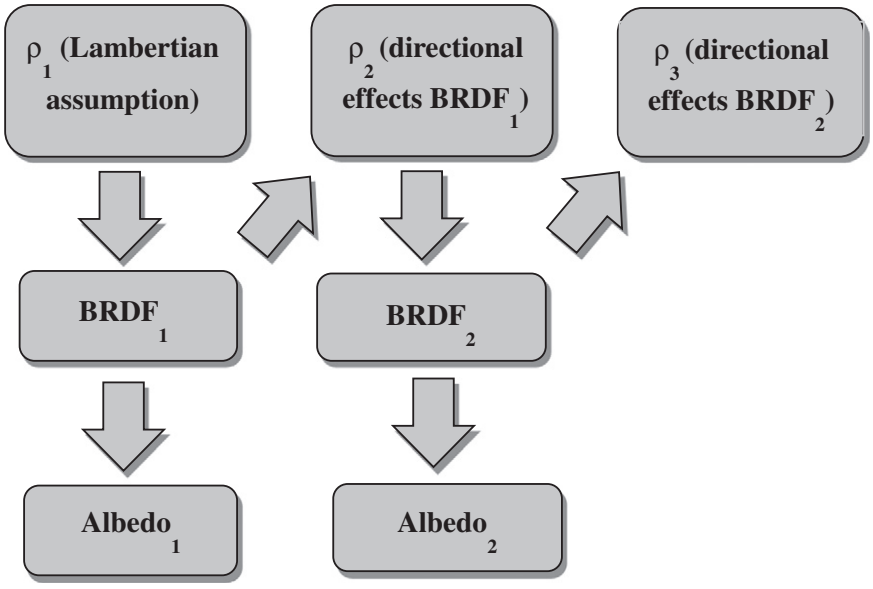

Fig. 2. Description of the methodology used in this work.

(Vermote et al., 1997). Eq. (3) is not analytically invertible to retrieve the surface reflectance since it is embedded in the integrals accounting for the coupling terms. However, this problem is solved in 6S by an iterative process. This process consists of using a BRDF model to perform the integrals in the coupling terms. Once the coupling terms are known, a new set of BRDF model coefficients is obtained. This is used again to update

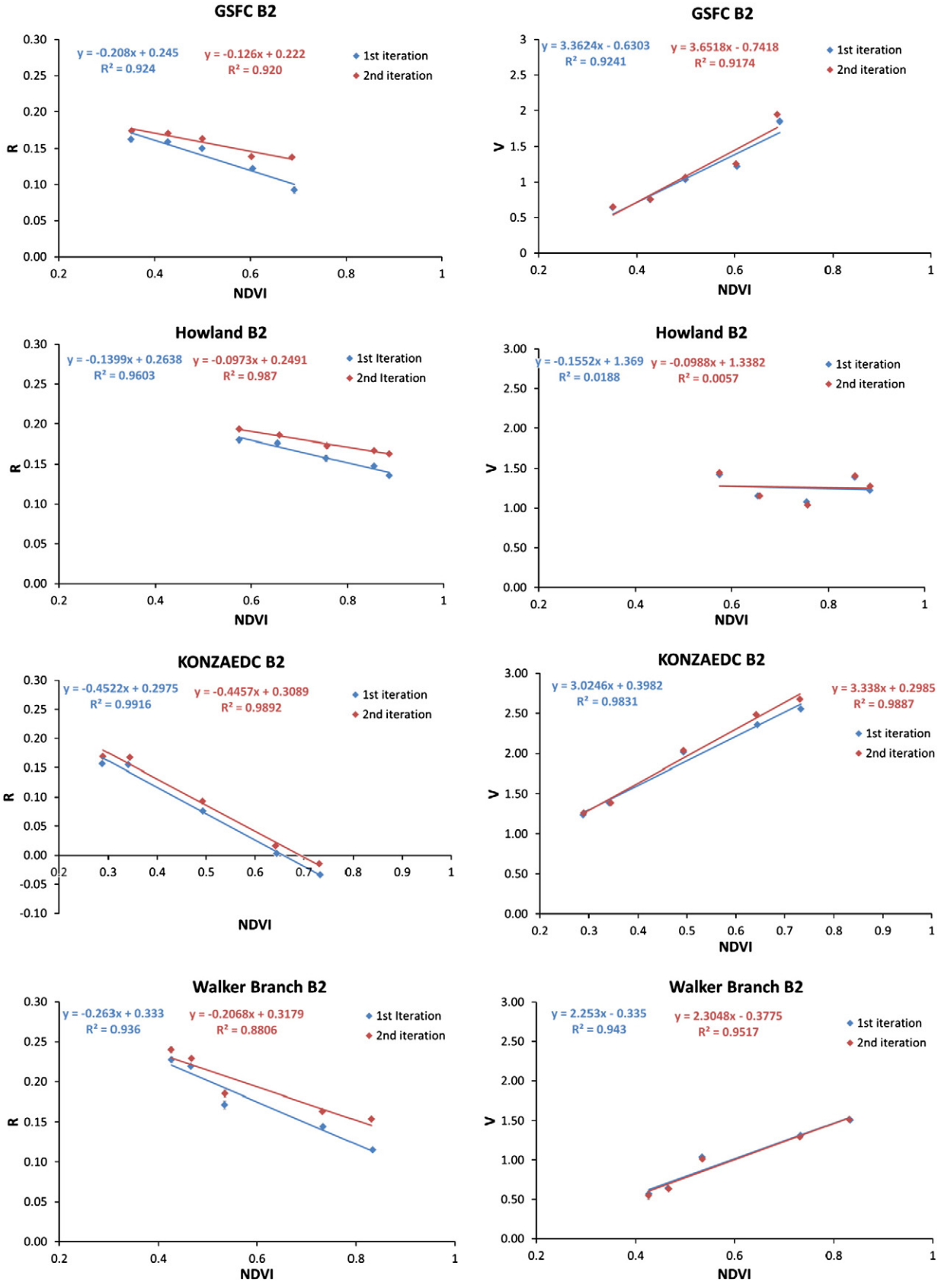

Fig. 3. Plots of the V and R parameters in band 2 versus the NDVI classes considered in each area in order to apply the Vermote et al. (2009) methodology.

the coupling terms and the subsequent coefficients. The procedure continues in this fashion until convergence is established.

Fig. 2 presents the methodology followed in this study. As described in the Study areas and dataset section, CMG data provides surface reflectance estimations. Therefore, first of all we inverted the atmospheric correction from these data in order to get to the L1B data. This process was carried out with the radiative transfer code 6S (Vermote et al., 2006) considering the surface as uniform and Lambertian. The necessary inputs in this process were the aerosol optical thickness at 550 nm, as well as the geometrical conditions of the pixel considered (day of the year, solar zenith angle, view zenith angle and relative azimuth angle). Additionally, we considered a continental aerosol model. Next, we estimated the surface reflectance (ρ_1) from raw data analogously as shown in the MODIS surface reflectance Algorithm Theoretical Background Document (ATDB, Vermote & Vermeulen, 1999) considering the surface as uniform and Lambertian. In this step we obtained the equivalent to the MODIS surface reflectance product (MOD09) from which we start, so the necessary inputs were the same as described in the inversion of the atmospheric correction. From this data we computed the BRDF model parameters ($BRDF_1$) and the albedo ($albedo_1$). Since these BRDF and albedo were derived from Lambertian data, we then use $BRDF_1$ in 6S in order to estimate the surface reflectance from raw data but considering the coupling between the BRDF and the downward radiance as shown in Eq. (3). We considered this surface reflectance, ρ_2, to retrieve a new BRDF ($BRDF_2$) and albedo ($albedo_2$). Finally, from $BRDF_2$ we estimated a final surface reflectance ρ_3.

The BRDF was estimated using a kernel-based BRDF model (Roujean et al., 1992). The theoretical basis of this semi-empirical model is that the land surface reflectance is modeled as a sum of three kernels representing basic scattering types: isotropic scattering, radiative transfer-type volumetric scattering as from horizontally homogeneous leaf canopies, and geometric-optical surface scattering as from scenes containing three-dimensional objects that cast shadows and are mutually obscured from view at off-nadir angles. Following Vermote et al. (2009), the surface reflectance (ρ) is written as:

$$\rho(\theta_s,\theta_v,\phi) = k_0\left[1+\frac{k_1}{k_0}F_1(\theta_s,\theta_v,\phi)+\frac{k_2}{k_0}F_2(\theta_s,\theta_v,\phi)\right] \quad (8)$$

where θ_s is the sun zenith angle, θ_v is the view zenith angle, F_1 is the volume scattering kernel, based on the Ross-Thick function derived by Roujean et al. (1992), but corrected for the hot-spot effect proposed by Maignan et al. (2004), and F_2 is the geometric kernel, based on the Li-sparse model (Li & Strahler, 1992) but considering the reciprocal form given by Lucht (1998). F_1 and F_2 are fixed functions of the observation geometry, but k_0, k_1, and k_2 are free parameters. Following this notation, we used V as k_1/k_0 and R for k_2/k_0. This BRDF model is used in the estimation of the MODIS MCD43 BRDF/albedo product (Strahler et al., 1999). Several studies have

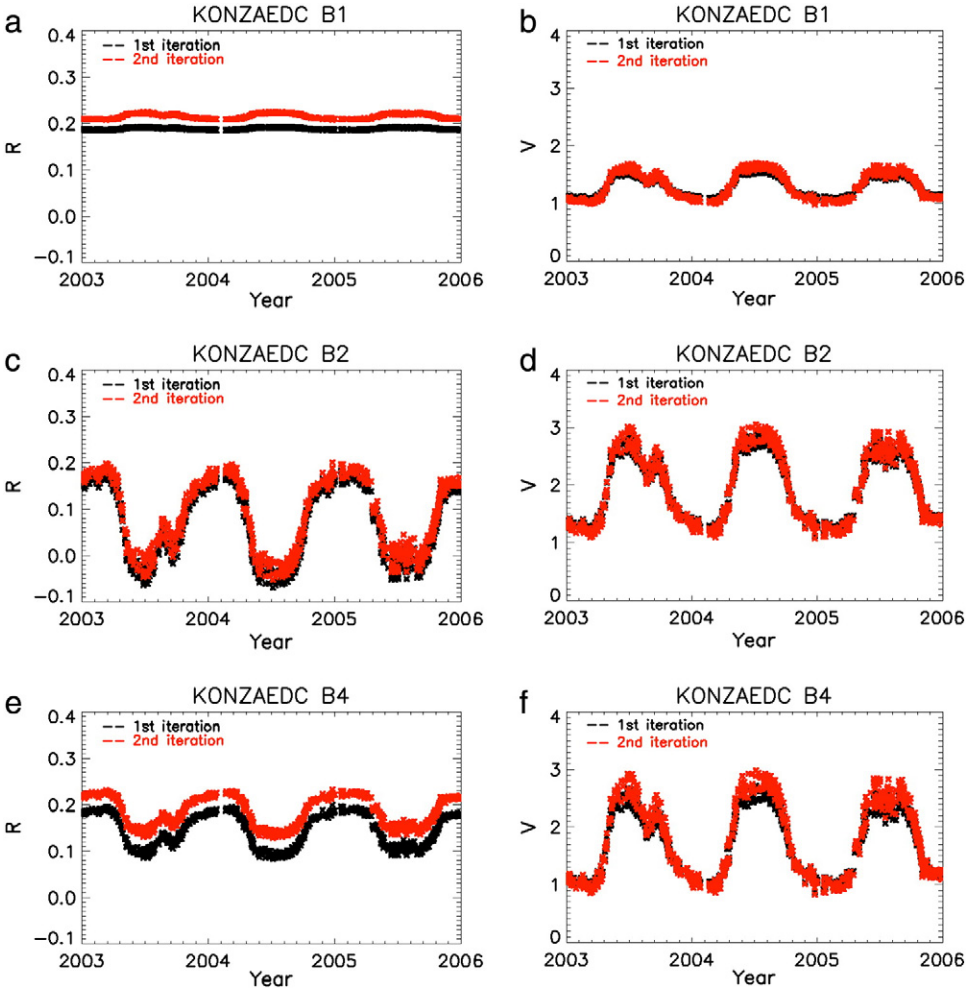

Fig. 4. Temporal evolution of R and V in band 1 (a and b), band 2 (c and d) and band 4 (e and f) of MODIS.

evaluated the MODIS MCD43 product accuracy using in situ data (Coddington et al., 2008; Jin et al., 2003; Liang et al., 2002; Liu et al., 2009; Roesch et al., 2004). These studies found a high correlation between in situ and satellite albedos for almost all cases concluding that the MODIS albedo product met an absolute accuracy requirement of 0.05.

For view-illumination geometries typical of medium-resolution sensors such as Terra and Aqua MODIS, in order to obtain enough bidirectional observations to retrieve the BRDF, a period of sequential measurements is usually needed to accumulate sufficient observations. As a result, the MCD43 product is estimated inverting the BRDF model parameters over a composite period of 16 days in which the surface is assumed to be stable. However, looking for an improvement in the albedo temporal resolution that avoided the assumption of a stable target, Vermote et al. (2009) presented a method that assumes that the BRDF shape variations through a year are limited and linked to the NDVI. This method permits more accurate tracking of events such as snow melt and vegetation phenology and retains the highest temporal resolution (daily, cloud cover permitting) without the noise generated by the day-to-day changes in observation geometry. This method has been recently compared to the MCD43 product by Bréon and Vermote (2012) for the correction of the surface reflectance time series. Their results showed that the performances of the two approaches are very similar, demonstrating that a simple four-parameter NDVI-scaled model performs as well as a more complex model with many more degrees of freedom. Following this methodology we segmented the whole dataset (three years of data) into five different classes of NDVI with equal population. We then inverted V and R (of each band) for each of these classes. After that, we generated a linear function that represented V and R as function of the NDVI. This led to a function (two coefficients) for each band and each of the two parameters to estimate V and R as a function of the NDVI. Lastly, we applied these functions to each NDVI image obtaining then instantaneous BRDF parameters.

Finally, the albedo was derived by integrals of the BRDF model through a simple parametrization by polynomials of the solar zenith angle (Strahler et al., 1999). The conversion from spectral to broadband albedo was achieved using the equation proposed by Liang (2000).

In the next section we show the results obtained when comparing ρ_1 with ρ_2 and ρ_3. With that aim we will estimate the Root Mean

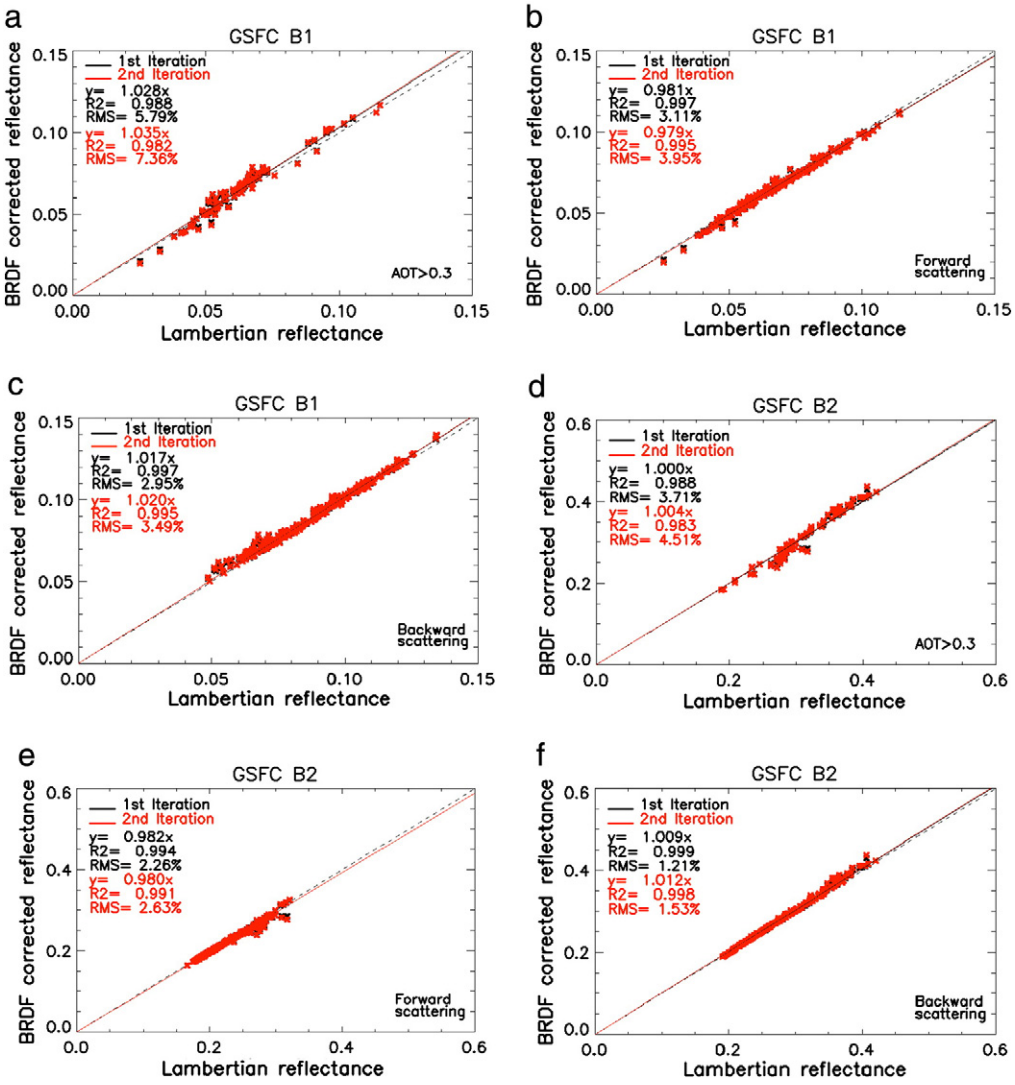

Fig. 5. Pixel-by-pixel comparison of BRDF corrected reflectance obtained from BRDF1 (first iteration, black) and from BRDF2 (second iteration, red) versus the Lambertian reflectance for GSFC site in band 1 (a,b,c), band 2 (d,e,f) and band 4 (g,h,i).

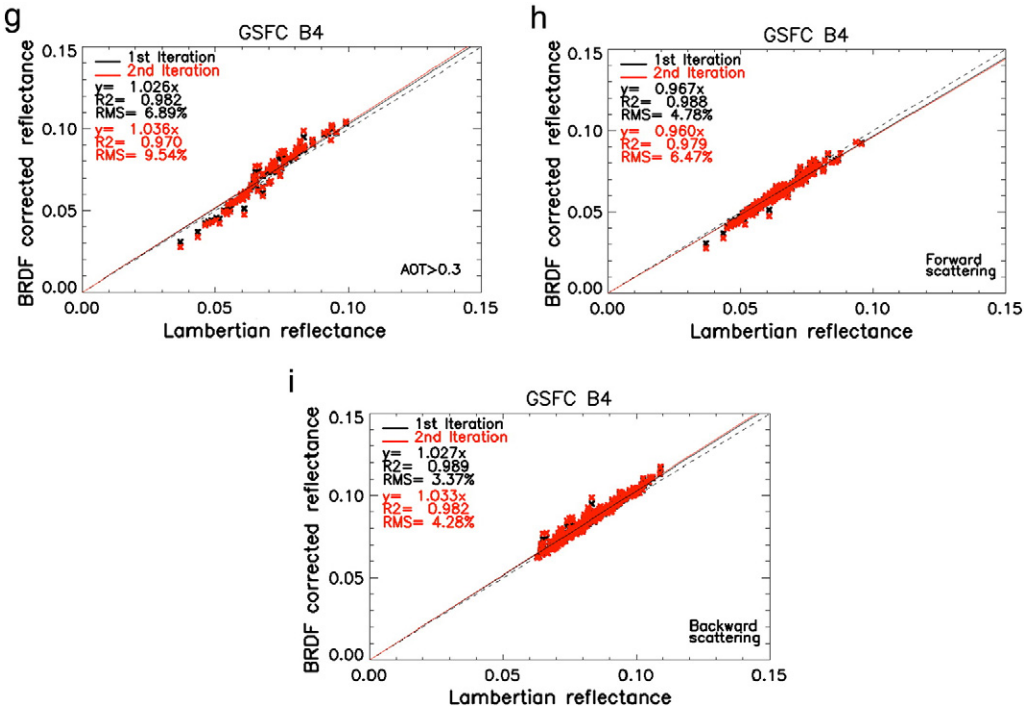

Fig. 5 (*continued*).

Square, *RMS*, relative error defined as:

$$RMS(\%) = \left[\frac{\sum_n \left(\frac{\rho_1 - \rho_{2,3}}{\rho_1} \right)^2}{n} \right]^{1/2}. \quad (9)$$

3. Results and discussion

Fig. 3 shows the V and R values in band 2 versus the NDVI classes that were estimated for each area in order to apply the methodology of Vermote et al. (2009). The plots show the expected increase of V and decrease of R with increasing NDVI. Additionally, the linear fit that allows the estimation of V and R parameters for each NDVI value through the time series presents a good correlation coefficient for every area except in the case of the V parameter in the Howland site. This particular area also presents the lowest variability of NDVI. Nevertheless, the standard deviation of the data was low and equal to 0.01. These plots also show that the difference between the first iteration and the second iteration is more noticeable in the R parameter than in V.

Fig. 4 presents the temporal evolution of V and R in the particular case of KONZAEDC. In this study we analyzed every MODIS band in the VNIR spectral range (band 1 to band 7), though, we just include band 1 (centered at 646.3 nm), band 2 (centered at 858.5 nm) and band 4 (centered at 553.7 nm) results, considering each one as representative of the red, near infrared and green spectral regions respectively. We have not included the blue band results as this band is used primarily for the aerosol retrievals (Vermote & Kotchenova, 2008). In Fig. 3 the first iteration (black) is referred to $BRDF_1$ parameters and the second iteration (red) to $BRDF_2$ parameters. These plots show that the difference between $BRDF_1$ and $BRDF_2$ is greater in bands 1 and 4 than in band 2. Also it is more noticeable in the parameter R than V. The analysis of the other bands leads to similar conclusions. The R parameter shows slightly negative values in band 2 during the summer. This is because the numerical solution of the least squares fit sometimes provides slightly negative (and unphysical) k_2 values. This parameter, which determines the magnitude of geometric and shadowing effects, is significant only when LAI is small (<0.5), and becomes negligible for larger LAI (Roujean et al., 1992).

Fig. 5 shows the pixel-by-pixel comparison of the BRDF corrected reflectance (ρ_2 and ρ_3) versus the Lambertian reflectance (ρ_1) for the GSFC site. We divided the analysis into three particular cases: high amount of aerosols (AOT > 0.3), forward scattering direction (relative azimuth angles greater than 90° but less than 270°) and backward

Table 1
Relative RMS when estimating the surface reflectance from a Lambertian assumption versus considering $BRDF_1$ (ρ_2) or $BRDF_2$ (ρ_3).

RMS (%)			AOT > 0.3	Forward scattering	Backward scattering
Howland	B1	ρ_2	7.5	3.9	2.0
		ρ_3	8.8	4.5	2.2
	B2	ρ_2	4.2	1.8	1.0
		ρ_3	4.7	2.0	1.1
	B4	ρ_2	9.5	5.9	2.8
		ρ_3	12.1	7.5	3.3
KONZA EDC	B1	ρ_2	6.3	3.3	2.2
		ρ_3	7.1	3.8	2.5
	B2	ρ_2	4.0	2.1	0.6
		ρ_3	4.3	2.2	0.7
	B4	ρ_2	7.6	5.0	2.3
		ρ_3	9.3	6.0	3.0
GSFC	B1	ρ_2	5.8	3.1	3.0
		ρ_3	7.4	4.0	3.5
	B2	ρ_2	3.7	2.3	1.2
		ρ_3	4.5	2.6	1.5
	B4	ρ_2	6.9	4.8	3.4
		ρ_3	9.5	6.5	4.3
Walker Branch	B1	ρ_2	5.8	3.0	2.9
		ρ_3	6.9	3.5	3.3
	B2	ρ_2	3.5	1.9	1.3
		ρ_3	4.0	2.1	1.5
	B4	ρ_2	7.4	4.9	3.5
		ρ_3	9.5	6.2	4.2

scattering direction (relative azimuth angles less than 90° and greater than 270°). The plots show a slope of regression near to one and a good correlation between the BRDF corrected and Lambertian reflectances. However, the slope as well as the error slightly increases for high amount of aerosols. Table 1 shows the RMS relative error (Eq. 9) for every site.

At first glance, the error committed when assuming a Lambertian surface is higher in band 1 (between 2% and 9%) and in band 4 (between 3% and 12%) than in band 2 (between 0.7% and 5%), which is in agreement with the variation in V and R between iterations presented in Fig. 4. The difference between ρ_2 and ρ_3 is less significant in bands 1 and 2 than band 4, where the difference is more noticeable and leads to the highest errors in ρ_3. Besides, the particular case of high amount of aerosols shows the highest errors when compared to the forward and backward scattering errors. Finally, regarding the two scattering directions, the largest errors are found with forward scattering. This might be because the atmosphere (especially the molecular scattering) scatters at large angles away from the forward direction (Vermote et al., 2006). Comparing the errors committed depending on each surface we observe that the highest errors correspond to the Howland pixel, while the other surfaces present similar results. This shows that the anisotropy correction does not depend on the heterogeneity of the surface (since GSFC is the most heterogeneous pixel and has similar errors as Walker Branch and KONZAEDC, which were homogeneous). Howland is situated in the north of the United States and during the winter has limited observations because of frequent cloud cover. Therefore, the particular case of Howland highest errors must be due to its limited number of observations and bad atmospheric conditions.

Next, we studied the impact of the BRDF correction on the NDVI. Fig. 6 shows the NDVI values obtained from $BRDF_2$ and $BRDF_3$ corrections versus the NDVI estimated considering the Lambertian assumption in case of the GSFC site. The plots show a good agreement between the different approaches with slopes near to one and low RMS. In this case, we did not observe any significant difference between the RMS values depending on the forward or backward scattering or for high aerosol amount, although this last case presented slightly higher errors. Additionally, the RMS between the first iteration and the second iteration (that is, considering $BRDF_2$ or $BRDF_3$) showed similar values. Table 2 shows the relative RMS estimated for every site. KONZAEDC presented the highest errors in case of high aerosol amounts which reached 2.6%. However, excepting this particular situation we obtained RMS values around 1%.

In order to evaluate the atmospheric effect, analogously to Hu et al. (1999), Fig. 7 displays the relative RMS between ρ_3 (considering it as the nearest to the true value) and (a) the top of atmosphere (TOA) reflectance, (b) ρ_1 and (c) ρ_2 versus the view zenith angle and for each zone. From these plots, we can see that the atmospheric effect is larger in band 4 (green) than in band 1 (red) and the lowest errors were obtained for band 2 (near infrared). This is a consequence of the decrease of the atmospheric scattering with wavelength and also of the larger effect of the atmospheric path radiance on the small reflectances of vegetated land covers (Walker Branch, Howland and KONZAEDC) in the red and green bands relative to its effect on their larger reflectances in the near infrared. Additionally, focusing on bands 1 and 4, we noticed higher errors in the forward scattering direction (indicated by negative view zenith angles) than in the backscattering direction, as we have seen in Table 1. This conclusion agrees with Lee and Kaufman (1986) where their results showed that the largest differences between the upward emerging radiance for a Lambertian surface versus for a non-Lambertian surface occurred in the backscattering region. However, they defined the backscattering direction for relative azimuth angles of 180°, which corresponds in our notation to the forward scattering direction. Centering our attention on the magnitude of the relative RMS obtained in Fig. 5b and Table 1, the errors are not higher than 8% in the red band and not higher than 12% in the green band. These values,

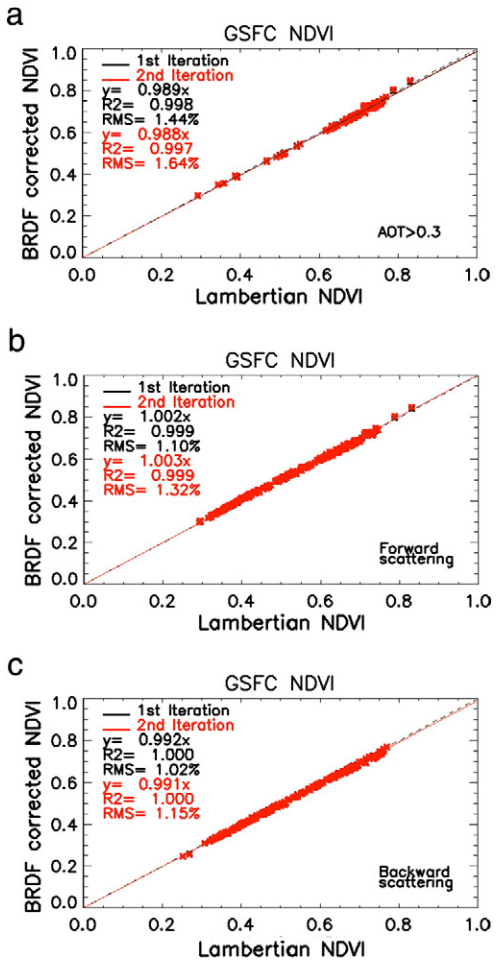

Fig. 6. Pixel-by-pixel comparison of BRDF corrected NDVI obtained from BRDF1 (first iteration, black) and from BRDF2 (second iteration, red) versus the Lambertian NDVI for GSFC site.

though, are lower than the Wang et al. (2010) results, which showed errors as high as 15% in the red band and 40% in the green band.

Fig. 8 shows the bias between ρ_3 and the TOA reflectance (a), ρ_1 (b) and ρ_2 (c) versus the view zenith angle for each zone. Band 4 presents the highest bias for TOA reflectances. For every zone and for bands 1 and 4, we obtain negative values that decrease (increase in absolute magnitude) for off-nadir view zenith angles. These results show that TOA reflectances overestimate the true reflectance value (ρ_3). However, band 2 presents much lower bias than bands 1 and 4 in TOA reflectances and leads to positive values. This is another result

Table 2
Relative RMS when estimating the NDVI from a Lambertian assumption versus considering $BRDF_1$ ($NDVI_2$) or $BRDF_2$ ($NDVI_3$).

RMS (%)		AOT > 0.3	Forward scattering	Backward scattering
Howland	$NDVI_2$	0.6	0.7	0.4
	$NDVI_3$	0.7	0.8	0.5
KONZA EDC	$NDVI_2$	2.2	1.4	1.1
	$NDVI_3$	2.6	1.7	1.3
GSFC	$NDVI_2$	1.4	1.1	1.0
	$NDVI_3$	1.6	1.3	1.2
Walker Branch	$NDVI_2$	0.6	0.8	0.7
	$NDVI_3$	0.7	0.9	0.8

that evidences the larger atmospheric effect over the visible region than the near infrared. Furthermore, centering our attention on the (b) and (c) plots we observe negative bias for negative view zenith angles (backscattering) and vice versa. These results lead to equivalent conclusions to Lee and Kaufman (1986), where they showed that the upward radiance for large solar zenith angles, in the backscattering direction (equivalent in our notation to the forward scattering) is larger for a Lambertian surface than for a non-Lambertian surface (overestimation). This effect also occurs (Fig. 8c) in case of considering the first iteration of the BRDF in the surface reflectance estimation (ρ_2) but the bias is reduced considerably. This underestimation at the forward scattering direction ($\rho_1 < \rho_3$) can be caused by the Ross-Thick component of the BRDF model since it is based on volumetric scattering of leaves which assumes that leaf transmittance equals leaf reflectance (Roujean et al., 1992) which is a fair assumption for the near infrared, but not for the visible bands.

Finally, we study the influence of considering the surface anisotropy in the surface albedo estimation. Under ideal conditions, albedo (an integrated function of BRDF) should not be highly impacted by the Lambertian errors because, as we have seen in Fig. 8b, the surface reflectance overestimation ($\rho_1 > \rho_3$) at the backward scattering plane will be compensated by its underestimation ($\rho_1 < \rho_3$) at the forward scattering plane.

Table 3 shows the relative RMS and the bias of the white sky albedo between its estimation from $BRDF_2$ ($albedo_2$) versus considering $BRDF_1$ ($albedo_1$) for every site. Analogously to Table 1, band 2 presents lower errors than bands 1 and 4 but, in this case, the difference is less significant than in the case of the surface reflectance. Additionally, the high amount of aerosols provides the highest RMS. The results show errors in the white sky albedo from 1.5 to 5.0% both in the red and the green bands and from 0.7 to 3.0% in the near infrared. Regarding the bias, we obtained negative values at every site and band, which implies that $albedo_1$ is greater than $albedo_2$. Additionally, band 2 shows the highest values which is due to its higher albedo than bands 1 and 4 in the case of vegetated sites.

Fig. 9 displays the relative RMS and the bias of the white sky broad band albedo between $albedo_2$ and $albedo_1$. From these plots we get RMS errors between 0.5 and 1.5% but there is no tendency depending on the view zenith angle. Furthermore, we obtain bias between −0.0015 and 0, being their values mostly negative independently of the site and the view zenith angle. This implies that in almost every case $albedo_1$ is greater than $albedo_2$, which is in contrast with the Wang et al. (2010) results, which showed that "Lambertian" albedo is slightly lower than the BRDF corrected albedo. In addition, we neither observe any tendency with the view zenith angle. Table 4 shows the relative RMS and the bias between $albedo_2$ and $albedo_1$ for every view zenith angle. The table shows similar RMS for every site of around the 1%, which agrees with Hu et al. (1999) and Lyapustin (1999) results. Additionally, we obtained a bias of around $-4 \cdot 10^{-4}$ in every zone except for KONZAEDC, which presents a higher bias of $10.3 \cdot 10^{-4}$.

4. Conclusions

In this paper, we have studied the influence of including the BRDF coupling in the atmospheric correction analyzing MODIS CMG data over four different sites. Several conclusions could be obtained from the study. Firstly, the effect of surface anisotropy is stronger in the green band (with errors from 3 to 12%) than the red band (with errors from 2 to 8%) and smaller in the near infrared band (with errors from 0.7 to 5.0%). However, these errors barely influence the NDVI estimation, obtaining relative RMS around 1%. Secondly, the difference between ρ_2 and ρ_3, that is, considering the first iteration ($BRDF_1$) or the second iteration ($BRDF_2$), is around 1–2% in the red band, 1–3% in the green band and almost insignificant (around 0.2%) in the near infrared. Thirdly, high amounts of aerosols lead to higher influence of the BRDF surface effects. Fourthly, we noticed higher errors in the forward scattering direction than in the backward scattering. Fifthly, the bias analysis showed that surface reflectance is overestimated in the forward scattering and is underestimated in the backward scattering when assuming a Lambertian surface.

On the other hand, regarding the albedo estimation, we obtain errors from 1.5 to 5.0% both in the red and the green bands and from 0.7 to 3.0% in the near infrared. In the case of the broad band white sky albedo, we obtained RMS errors around the 1% which agrees with previous works. Additionally, we get small negative bias values (from $-4 \cdot 10^{-4}$ until $-10 \cdot 10^{-4}$), which indicate that the Lambertian assumption only generates a slight overestimation of the albedo.

To sum up, in future works the assumption of Lambertian surface can be used satisfactorily in the derivation of surface reflectance and surface albedo. In fact, the obtained RMS of 1% in case of the surface albedo estimation meets the accuracy requirement of 5% suggested by Global Climate Observing System (GCOS) (2006). However, it should be used carefully for high aerosol amounts since this can result in a significant error in the surface reflectance estimation.

Acknowledgments

The authors would like to thank the Spanish Ministerio de Innovación y Ciencia (EODIX, project AYA2008-0595-C04-01; CEOS-Spain, project AYA2011-29334-C02-01) in addition to the European Union (CEOP-AEGIS, project FP7-ENV-2007-1 proposal No. 212921; WATCH, project 036946) for supporting the work presented in this paper.

References

Barnsley, M. J., Allison, D., & Lewis, P. (1997). On the information content of multiple-view-angle (MVA) data sets. *International Journal of Remote Sensing*, *18*, 1937–1960.

Bréon, F. M., & Vermote, E. F. (2012). Correction of MODIS surface reflectance time series for BRDF effects. *Remote Sensing of Environment*, *125*, 1–9.

Coddington, O., Schmidt, K. S., Pilewskie, P., Gore, W. J., Bergstrom, R. W., Roman, M. O., Redemann, J., Russell, P. B., Liu, J., & Schaaf, C. B. (2008). Aircraft measurements ofspectral surface albedo and its consistency with ground-based and space-borne observations. *Journal of Geophysical Research*, *113*, D17209. http://dx.doi.org/10.1029/2008JD010089.

Global Climate Observing System (GCOS) (2006). *Systematic observation requirements for satellite-based products for climate*. Supplemental details to the satellite-based component of the "Implementation Plan for the Global Observing System for Climate in Support of the UNFCCC". September 2006 GCOS-107 (WMO/TD No. 1338).

Holben, B. N., Eck, T. F., Slutsker, I., Tanré, D., Buis, J. P., Setzer, A., Vermote, E., Reagan, J. A., Kaufman, Y. J., Nakajima, T., Lavenu, F., Jankowiak, I., & Smirnov, A. (1998). AERONET—A federated instrument network and data archive for aerosol characterization. *Remote Sensing of Environment*, *66*, 1–16.

Hu, B., Lucht, W., & Strahler, A. (1999). The interrelationship of atmospheric correction of reflectances and surface BRDF retrieval: A sensitivity study. *IEEE Transactions on Geoscience and Remote Sensing*, *37*, 724.

Huete, A., Justice, C., & van Leeuwen, W. (1999). MODIS Vegetation Index, Algorithm Theoretical Basis Document (ATDB) Version 3, University of Arizona. online at:. http://modis.gsfc.nasa.gov/data/atbd/atbd_mod13.pdf

Jin, Y., Schaaf, C. B., Gao, F., Li, X., Strahler, A. H., Lucht, W., & Liang, S. (2003). Consistency of MODIS surface BRDF/Albedo retrieval. 1: Algorithm performance. *Journal of Geophysical Research*, *108*(D5), 4158.

Kriebel, K. T. (1978). Measured spectral bidirectional reflection properties of four vegetated surfaces. *Applied Optics*, *17*(2), 253–259.

Lee, T., & Kaufman, Y. J. (1986). Non-Lambertian effects on remote sensing of surface reflectance and vegetation index. *IEEE Transactions on Geoscience and Remote Sensing*, *GE-24*(5), 699–708.

Li, X., & Strahler, A. H. (1992). Geometric-optical bidirectional reflectance modelling of the discrete crown vegetation canopy: Effect of crown shape and mutual shadowing. *IEEE Transactions on Geoscience and Remote Sensing*, *30*, 276–292.

Liang, S. (2000). Narrowband to broadband conversions of land surface albedo. I Algorithms. *Remote Sensing of Environment*, *76*, 213–238.

Liang, S., Fang, H., Chen, M., Shuey, C., Walthall, C., Doughtry, C., Morisette, J., Schaaf, C., & Strahler, A. (2002). Validating MODIS land surface reflectance and albedo products: Methods and preliminary results. *Remote Sensing of Environment*, *83*, 149–162.

Liu, J., Schaaf, C. B., Strahler, A. H., Jiao, Z., Shuai, Y., Zhang, Q., Roman, M., Augustine, A., & Dutton, E. G. (2009). Validation of Moderate Resolution Imaging Spectroradiometer (MODIS) albedo retrieval algorithm: Dependence of albedo on solar zenith angle. *Journal of Geophysical Research-Atmospheres*, *114*, D01106.

Lucht, W. (1998). Expected retrieval accuracies of bidirectional reflectance and albedo from EOS-MODIS and MISR angular sampling. *Journal of Geophysical Research*, *103*, 8763–8778.

Lyapustin, A. (1999). Atmospheric and geometrical effects on land surface albedo. *Journal of Geophysical Research*, *104*, 4127–4144.

Lyapustin, A., Wang, Y., Martonchik, J., Privette, J., Holben, B., Slutsker, I., Sinyuk, A., & Smirnov, A. (2006). Local analysis of MISR surface BRF and albedo over GSFC and Mongu AERONET sites. *IEEE Transactions on Geoscience and Remote Sensing*, *44*, 1707–1718.

Maignan, F., Breon, F. M., & Lacaze, R. (2004). Bidirectional reflectance of Earth targets: Evaluation of analytical models using a large set of space-borne measurements with emphasis on Hot-Spot. *Remote Sensing of Environment*, *9*, 210–220.

Morisette, J. T., Privette, J. L., & Justice, C. O. (2002). A framework for the validation of MODIS Land products. *Remote Sensing of Environment*, *83*, 77–96.

Roesch, A., Schaaf, C., & Gao, F. (2004). Use of Moderate-Resolution Imaging Spectroradiometer bidirectional reflectance distribution function products to enhance simulated surface albedos. *Journal of Geophysical Research*, *109*, D12105. http://dx.doi.org/10.1029/2004JD004552.

Roujean, J. -L., Leroy, M., & Deschamps, P. Y. (1992). A bidirectional reflectance model of the Earth's surface for the correction of remote sensing data. *Journal of Geophysical Research*, *97*, 20455–20468.

Strahler, A. H., Lucht, W., Schaaf, C. B., Tsang, T., Gao, F., Li, X., Muller, J. -P., Lewis, P., & Barnsley, M. J. (1999). *MODIS BRDF albedo product: Algorithm theoretical basis document, NASA EOS-MODIS Doc., V5.0.*

Tanré, D., Herman, M., & Deschamps, P. Y. (1983). Influence of the atmosphere on space measurements of directional properties. *Applied Optics*, *21*, 733–741.

Vermote, E., Justice, C., & Bréon, F. M. (2009). Towards a generalized approach for correction of the BRDF effect in MODIS directional reflectances. *IEEE Transactions on Geoscience and Remote Sensing*, *47*, 3898–3908.

Vermote, E. F., & Kotchenova, S. (2008). Atmospheric correction for the monitoring of land surfaces. *Journal of Geophysical Research*, *113*, D23S90. http://dx.doi.org/10.1029/2007JD009662.

Vermote, E. F., Tanré, D., Deuzé, J. L., Herman, M., & Morcrette, J. J. (1997). Second simulation of the satellite signal in the solar spectrum, 6S: An overview. *IEEE Transactions on Geoscience and Remote Sensing*, *35*(3), 675–686.

Vermote, E. F., Tanre, D., Deuze, J. L., Herman, M., Morcrette, J. J., Kotchenova, S. Y., & Miura, T. (2006). *Second simulation of the satellite signal in the solar spectrum (6S), 6S user guide version 3 (November, 2006).* http://www.6s.ltdri.org

Vermote, E. F., & Vermeulen, A. (1999). Atmospheric correction algorithm: Spectral reflectances (MOD09). Algorithm Theoretical Background Document. available on line at. http://modarch.gsfc.nasa.gov/MODIS/ATBD/atbd_mod08.pdf

Wang, Y., Lyapustin, A., Privette, J. L., Cook, R. B., SanthanaVannan, S. K., Vermote, E. F., & Schaaf, C. L. (2010). Assessment of biases in MODIS surface reflectance due to Lambertian approximation. *Remote Sensing of Environment*, *114*, 2791–2801.

Wang, Y., Lyapustin, A. I., Privette, J. L., Morisette, J. T., & Holben, B. (2009). Atmospheric correction at AERONET locations: A new science and validation dataset. *IEEE Transactions on Geoscience and Remote Sensing*, *47*(8), 2450–2466.

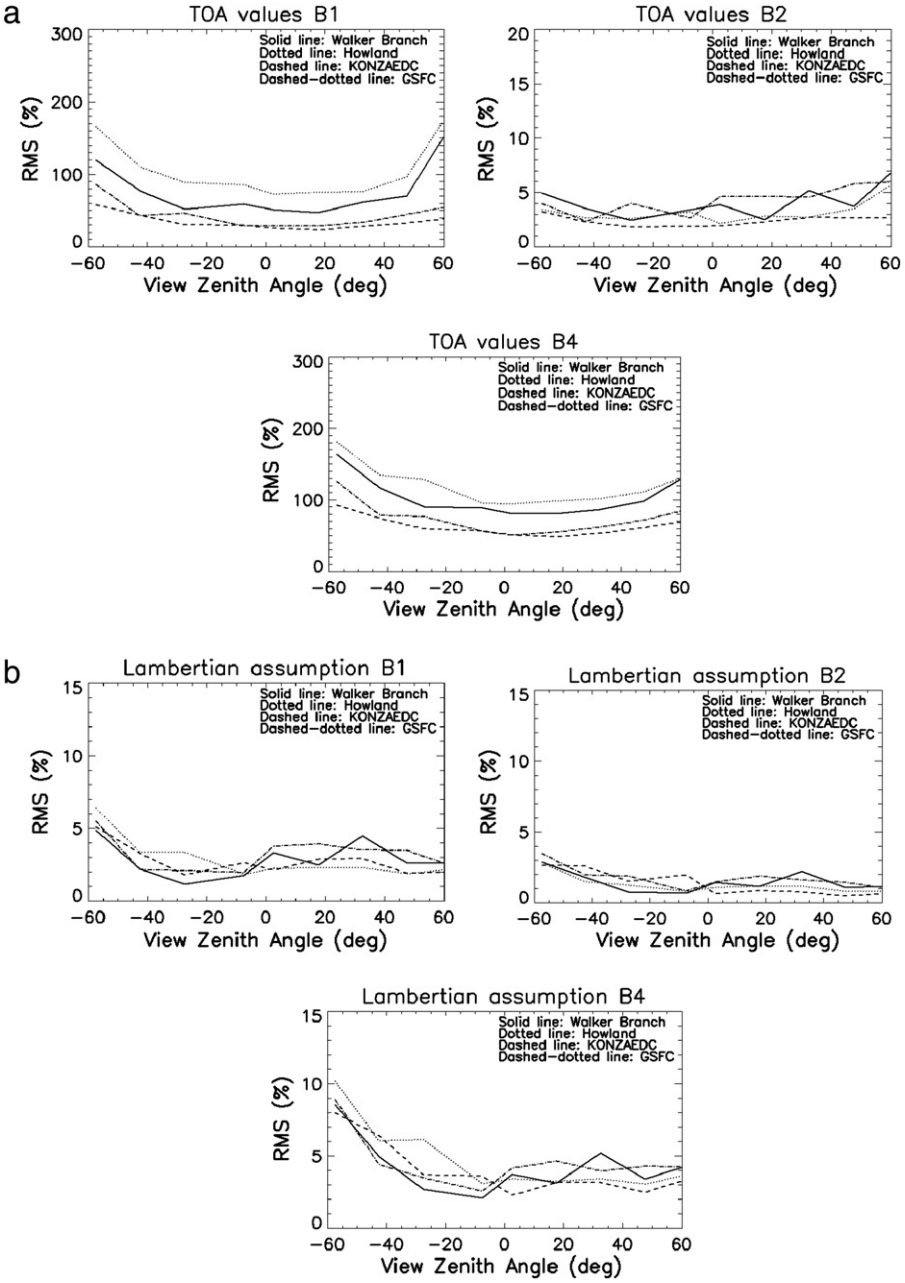

Fig. 7. Relative RMS between ρ_3 (considering it as the nearest to the true value) and (a) the top of atmosphere (TOA) reflectance, (b) ρ_1 and (c) ρ_2 versus the view zenith angle and for each zone.

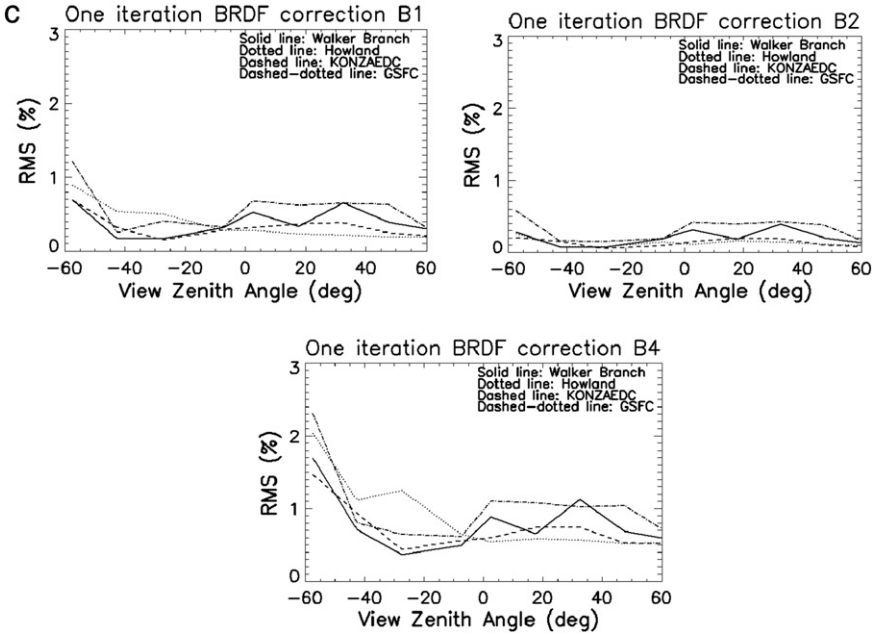

Fig. 7 (*continued*).

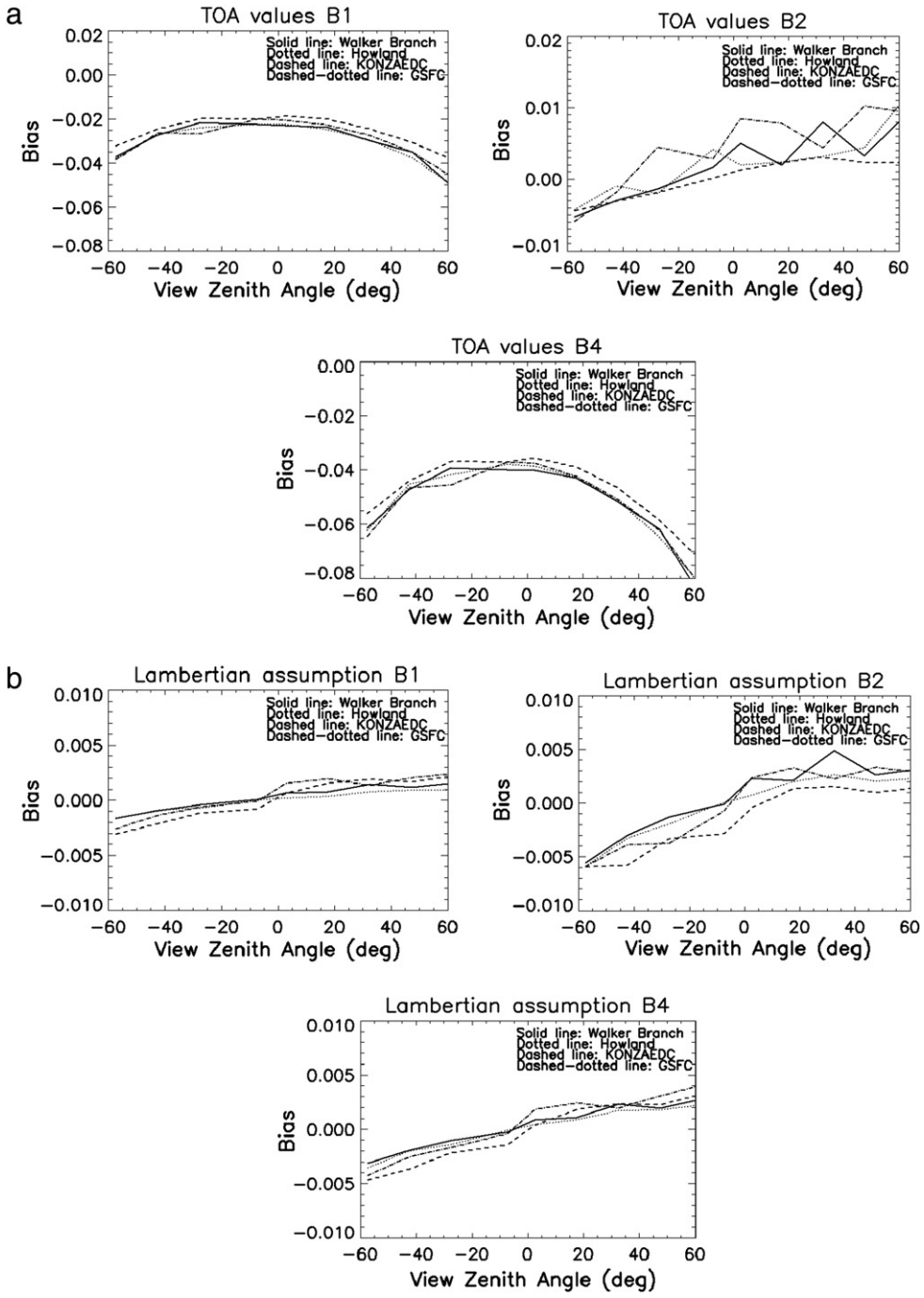

Fig. 8. Bias obtained considering the average of ρ_3 minus a) top of atmosphere reflectances, b) ρ_1 and c) ρ_2 versus the view zenith angle and for each zone.

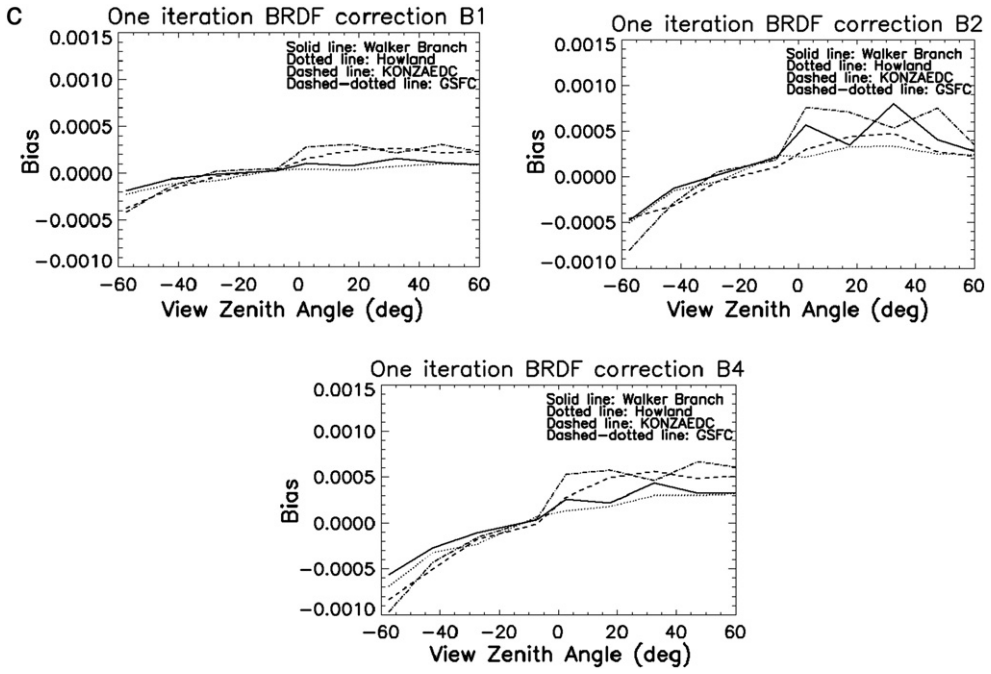

Fig. 8 (*continued*).

Table 3
Relative RMS when estimating the white sky albedo from $BRDF_2$ ($albedo_2$) versus considering $BRDF_1$ ($albedo_1$).

RMS (%)		AOT > 0.3	Forward scattering	Backward scattering	Bias $(albedo_2 - albedo_1) \cdot 10^{-4}$
Howland	B1	5.0	2.2	1.7	−0.01
	B2	2.9	1.1	0.8	−11.6
	B4	4.7	2.0	1.2	−0.7
KONZA EDC	B1	3.8	1.4	0.8	−4.5
	B2	3.1	1.2	0.9	−22.2
	B4	3.9	1.5	1.0	−6.4
GSFC	B1	2.2	1.3	1.5	−0.9
	B2	1.8	1.1	1.3	−10.3
	B4	2.1	1.4	1.6	−1.3
Walker Branch	B1	2.3	1.3	1.4	−0.9
	B2	1.9	1.1	1.0	−12.9
	B4	2.6	1.6	1.5	−1.5

Table 4
RMS and bias of the white sky broad band albedo when comparing $albedo_1$ to $albedo_2$.

	Howland	KONZA EDC	GSFC	Walker Branch
RMS (%)	1.00	0.97	1.07	1.01
Bias $(albedo_2 - albedo_1)$	$-4.7 \cdot 10^{-4}$	$-10.3 \cdot 10^{-4}$	$-3.9 \cdot 10^{-4}$	$-4.5 \cdot 10^{-4}$

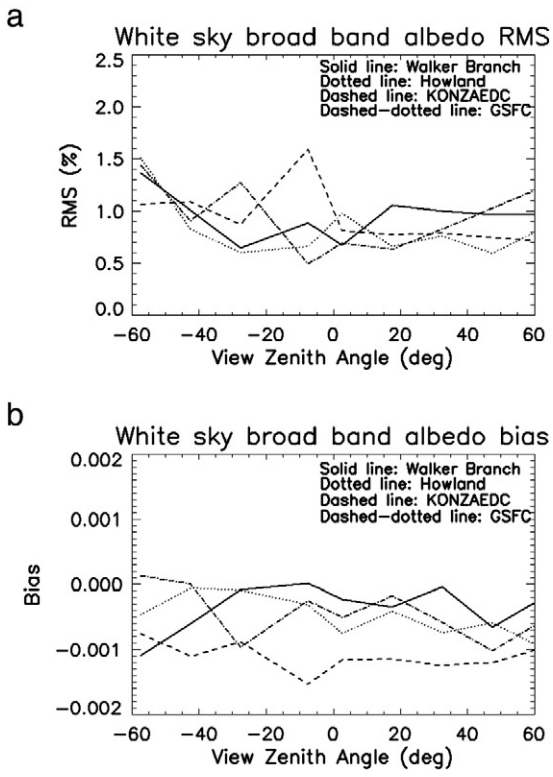

Fig. 9. White sky broad band albedo relative RMS (a) and bias (b) obtained comparing the $albedo_2$ to $albedo_1$ for each site.